J. Phys. B: At. Mol. Opt. Phys. **40** (2007) 4551–4560 doi:10.1088/0953-4075/40/24/001

Infrared emission spectrum and potentials of 0_u^+ and 0_g^+ states of Xe_2 excimers produced by electron impact

A F Borghesani[1,2], **G Carugno**[2] **and I Mogentale**[1,2]

[1] Department of Physics, University of Padua, Italy
[2] I. N. F. N., Sezione di Padova, via F. Marzolo 8, I-35131 Padua, Italy

E-mail: borghesani@padova.infm.it

Received 6 June 2007, in final form 2 October 2007
Published 19 November 2007
Online at stacks.iop.org/JPhysB/40/4551

Abstract

We present an investigation of the Xe_2 excimer emission spectrum observed in the near-infrared range about 7800 cm^{-1} in pure Xe gas and in an Ar (90%)–Xe (10%) mixture for $P = 0.1$ MPa at $T = 300$ K obtained by exciting the gas with energetic electrons. The Franck–Condon simulation of the spectrum shape suggests that the emission stems from a bound–free molecular transition never studied before. The states involved are assigned as the bound $(3)0_u^+$ state related to the $6p[1/2]_0$ atomic limit and the dissociative $(1)0_g^+$ state with the $6s[3/2]_1$ limit. A comparison with the spectrum simulated by using theoretical potentials for internuclear distances over which the vibrational eigenfunctions of the bound state have non-negligible amplitude shows that the dissociative potential does not reproduce correctly the spectrum features. A best fit, purely repulsive potential is thus proposed to accurately reproduce the observed spectrum.

The vacuum ultraviolet (VUV) luminescence of Xe excimers has been thoroughly investigated because of its importance for realizing intense sources of coherent and incoherent VUV radiation [1]. This property of Xe is also exploited, for instance, to build high-energy particle detectors in which ionizing particles passing through a Xe-filled ionization chamber produce VUV scintillation light [2].

Actually, all investigations on Xe excimers are devoted to explaining the processes leading to the emission of the two VUV continua observed under different experimental conditions in gas excited by discharges [3], UV photons [4, 5], multiphotons [6, 7] or high-energy particles [8–11].

Radiative transitions from the vibrationally excited $\left(0_u^+\right)_{v'\gg 0}$ molecular state, correlated with the resonant $6s(^3P_1)$ atomic state, to the dissociative 0_g^+ ground state produce the first continuum at 152 nm. The second continuum at 170 nm consists of the overlapping bound–free emission from the lowest vibrationally relaxed $(0_u^-, 1_u)$ molecular states correlated with the metastable $6s(^3P_2)$ atomic state [6, 11].

The observation that the Xe VUV luminescence is due to the first continuum at low gas pressure ($P < 2 \times 10^4$ Pa) whereas it consists of the second continuum for $P > 5 \times 10^4$ Pa is explained by the different kinetics of the processes leading to excimer formation and decay [12]. Mainly metastable atomic and gerade (g) molecular states are studied because of their involvement in these processes [13], whose kinetics has been clarified in several spectral- and time-resolved experiments in which lifetimes and rate constants have been determined [6, 10–12, 14–21]. The structure of the lowest lying excited molecular states has been investigated theoretically with *ab initio* [22, 23] or model [24] calculations of the molecular potentials and experimentally by analysing spectroscopic data [6, 9, 15, 25, 26].

Until now, however, researchers have almost neglected the possibility that, in the cascade of processes leading to VUV emission, molecular transitions occur in the infrared (IR) range. There is only scant indication [27] of a broad IR spectrum occurring in the range 765–830 nm, more precisely in the range 780–815 nm [28], which is attributed to a bound–bound transition from vibrational levels of the molecular 0_g^+ state correlated with the $6p[1/2]_0$ atomic limit to the $B0_u^+(6s[3/2]_1)_{v'\gg 0}$ molecular state in a highly excited vibrational level.

No further measurements of molecular IR emission are found in the literature. Their absence might be due to the fact the potential energy minimum of higher lying, bound excimer states occurs at an internuclear distance at which the weakly bound ground-state potential is strongly repulsive. For this reason, these molecular states are not easily reached by multiphoton selective excitation. By contrast, broad-band excitation using high-energy, charged particles [10, 29] produces excited atoms with such high kinetic energy that can collide at a short distance with ground-state atoms yielding higher lying excimer states. The price to be paid, however, is that the parity of the molecular states produced in this way cannot be controlled.

Recently, we observed for the first time a broad molecular emission spectrum centred at $\lambda \approx 1.3\ \mu$m ($\tilde{\nu} \approx 7860\ \text{cm}^{-1}$) in both pure Xe gas and in a Xe (10%)−Ar(90%) mixture at room temperature and at a pressure $P = 0.1$ MPa by exciting the gas with a pulsed beam of 70 keV electrons [30]. Details of the technique can be found in the literature. It is only worth recalling here that we use a Fourier-transform-IR (FT-IR) spectrometer in a stepscan mode [31]. An InGaAs photodiode with flat responsivity in the range $(0.6 \leqslant \tilde{\nu} \leqslant 1.2) \times 10^4 \text{cm}^{-1}$ was used as the detector.

As we were then interested on the behaviour of the excimer emission as a function of the gas density in order to study the excimer interaction with a high density environment [32] to explore the feasibility of a high-energy particles detector based on this IR luminescence, we attributed the emission to a Xe_2 bound–free transition between a state dissociating into the 6p manifold and one of 6s configuration without any further inquiries, also because accurate potential energy curves for those high-lying states were not available.

Meanwhile, an extensive set of Xe_2 molecular potential energy curves has been published [23] that fully span the energy range in which the IR molecular emission discovered by us occurs.

In the present paper, we report new and more accurate high-resolution, time-integrated measurements of the IR emission spectrum of Xe_2 that allow, for the first time, a more precise assignment of the molecular states involved in the transition. This goal is accomplished by comparing the observed spectrum with the spectrum calculated by exploiting the new theoretical potentials of the higher molecular states.

We have used the same FT-IR spectrometer operated in a stepscan mode, but at higher resolution than in the previous experiment [30]. Moreover, we have replaced the InGaAs detector with a liquid-N_2 cooled InSb photodiode detector in order to extend the explored wave number range towards the red side of the spectrum. In figure 1, we show the IR spectrum recorded in an extended wave number range with 16 cm^{-1} resolution in pure Xe gas at $P = 0.1$

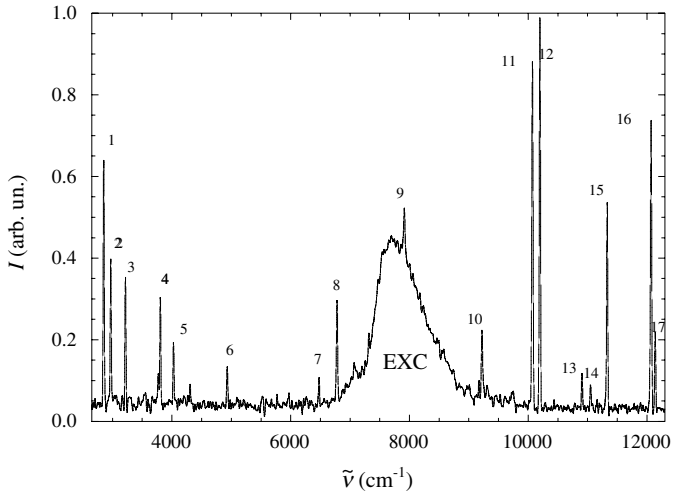

Figure 1. The IR emission spectrum of electron-impact excited Xe gas at $P = 0.1$ MPa at room temperature. The broad continuum (labelled EXC) is the excimer spectrum. Xe I atomic lines are numbered (see text).

MPa and $T \approx 300$ K. The excimer emission band appears in the centre of the figure and is surrounded by several atomic lines of Xe I. The full width at half maximum (FWHM) is $\Gamma \approx 900$ cm^{-1}. Its value relative to the wave number $\tilde{\nu}_m$ of the centre of the excimer band is $\Gamma/\tilde{\nu}_m \approx 0.115$ and is comparable with the value 0.116 of the second VUV continuum [8, 33]. In the limit of low pressure, $\tilde{\nu}_m$ and Γ are the same both in the pure gas and in the Xe (10%)–Ar (90%) mixture, thus showing that the same species, namely Xe_2, is emitting in both cases [30].

An analysis of the Xe I atomic lines surrounding the molecular band sheds light on what atomic states the emitting excimer is correlated with. By referring to the numbers labelling the atomic lines in figure 1, we observe that lines 1 through 6 stem from 5d–6p transitions. In particular, line 1 is the well-known Xe I line at $\lambda = 3.51$ μm [34]. Lines 7 through 9 are 7s–6p transitions. Lines 10 through 12 are emitted in 6p–6s transitions. Line 13 is actually an unresolved 6p–6s and 6d–6p doublet. Line 14 is due to a 6s–5p transition and, finally, lines 15 through 17 are 6p–5p transitions[3].

The presence in this wave number region of lines associated with 6p atomic states provides evidence that states in the 6p manifold are efficiently populated in the deexcitation processes occurring after electron-impact excitation of the gas. Moreover, the presence of 7s–6p lines very close to, or embedded in, the excimer band suggests that the upper bound molecular state is related to a state in the 6p manifold. In particular, line 9 is due to a transition from the $7s[1/2]^0$ atomic state (in Racah notation) to the $6p[1/2]_0$ one (see footnote 3). Thus, we reasonably assume that the bound molecular state is correlated with this latter limit.

At the density of the present experiment, $N \approx 2.4 \times 10^{25}$ m^{-3}, the mean free time between collisions is estimated to be $\tau_c \approx 10^{-11}$ s [30]. The three-body quenching of the $6p[1/2]_0$ state observed by Bőwering *et al* [35] suggests that a molecular bound state correlated with this atomic limit could efficiently be populated by a collisional-induced association which is a three-body process [12]. By contrast, the predissociation time of the bound molecular state to

[3] http://physics.nist.gov/PhysRefData/ASD/index.html.

the $5d[1/2]_1$ limit is estimated to be $\tau_p \approx 10^{-10}$ s [7, 12]. The large collision rate thus leads to a quick electronic relaxation of the excimer which would otherwise predissociate.

At present, there are no estimates for the radiative lifetime and decay rate for vibrational relaxation for this molecular bound state. We assume that they do not differ too much from those of the states responsible for the VUV continua. The radiative lifetimes of highly excited vibrational states of the 0_g^+ and $(1_u, 0_u^-)$ excimers are estimated to be $\tau_1 \approx 5$ ns [13] and $\tau_2 \approx 40$ ns [9], respectively. The decay rate for vibrational relaxation k_3 has the same value for all states [18], yielding a decay time $\tau_3 = (k_3 N)^{-1} \approx 0.65$ ns at the present density. In any case, as τ_c is much shorter than all other characteristic times, we assume that collisions stabilize excimers electronically and also quickly establish thermal equilibrium.

The simulation of the line shape by means of Franck–Condon calculations for the presently assumed bound–free transition requires the knowledge of the potential energy curves of the initial and final molecular states and of the transition moment as a function of the internuclear distance R. Theoretical calculations of the molecular potentials for higher lying states have appeared recently [23], whereas calculations for the transition moments of such higher-lying molecular states are still missing.

The choice of the potentials has to fulfil the following criteria: (i) the upper bound state has to be related to the atomic 6p manifold; (ii) the selection rule for state parity, $u \leftrightarrow g$ and ${}^+\leftrightarrow{}^+$, must be obeyed; (iii) the energy difference between the potential energy curves at the equilibrium distance of the bound state must approximately be equal to $\tilde{\nu}_m$.

These criteria are met by the choice of the ungerade state $(3)0_u^+$ correlated with the $6p(^1D_2)$ atomic limit for the bound state and of the gerade $(1)0_g^+$ correlated with the $6s(^3P_1)$ limit as the dissociative state [23]. As a transition $0_u^+ \rightarrow 0_g^+$ is involved, conservation of the total angular momentum enforces the additional selection rule $\Delta J = \pm 1$ [36].

Though the potential energy curves are known, nonetheless several approximations must still be done in order to carry out numerical calculations. First of all, as the transition moment for the states considered here is not known, we assume that it does not vary too rapidly as a function of the internuclear distance R and calculate the line shape within the *centroid approximation* [36, 37], thus yielding for the intensity I of the spectrum the following expression:

$$I \propto \sum_{v'J'} \mathrm{e}^{-\beta E_{v'J'}} \{(J'+1)|\langle \epsilon'', J'+1|v', J'\rangle|^2 + J'|\langle \epsilon'', J'-1|v', J'\rangle|^2\} \tilde{\nu}^4, \tag{1}$$

in which the selection rule $\Delta J = J'' - J' = \pm 1$ has been used. As usual, primed quantities refer to the upper state whereas doubly primed quantities refer to the lower state. $\beta = (k_\mathrm{B} T)^{-1}$, where k_B is the Boltzmann constant and T is the gas temperature.

$\tilde{\nu}$ is the emission wave number and is defined as

$$\tilde{\nu} = [(T_e' - T_e'' - D_e'') + E_{v'J'} - \epsilon'']. \tag{2}$$

Here, T_e' and T_e'' are the values of the minimum of the potential energy curves of the upper and lower states, respectively. They are measured with respect to the situation in which two ground-state Xe atoms are at infinite separation with zero kinetic energy [23, 38]. D_e'' is the well depth of the lower potential. In fact, though mainly repulsive, the potential energy curve of the $(1)0_g^+$ state has a weak van der Waals minimum for large R [23].

$E_{v'J'}$ is the energy of a rovibrational state $|v', J'\rangle$ of the bound potential described by the vibrational quantum number v' and by the rotational quantum number J':

$$E_{v'J'} = E_{v'} + E_{J'}. \tag{3}$$

Here, $E_{v'}$ are the vibrational energy eigenvalues of the bound potential measured from the bottom of the potential well and $E_{J'}$ are the rotational energy eigenvalues.

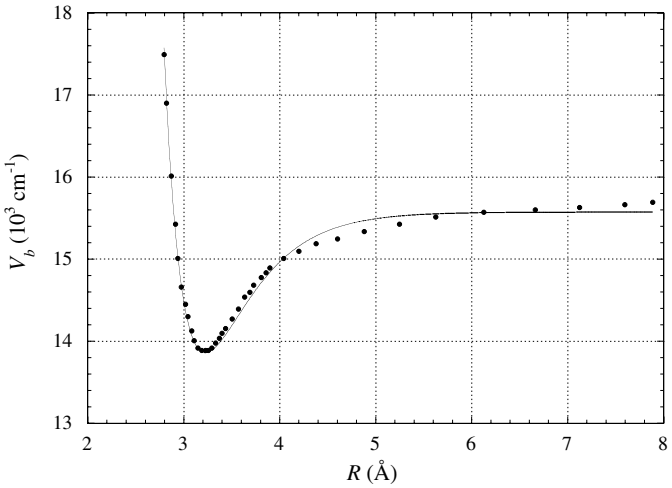

Figure 2. Potential energy curve for the $(3)0_u^+$ state. Dots: literature data [23]. Curve: Morse fit.

The decoupling of the vibrational and rotational energies in (3) can be accomplished because vibrations are far more energetic than rotations. Moreover, as the amplitude of vibrations is much smaller than the average internuclear distance, it is surely a good approximation to express the contribution from the rotational energy, which is proportional to R^{-2}, through the replacement of R^2 by $R_{e'}^2$ [38], where $R_{e'}$ is the equilibrium internuclear distance of the bound state $(3)0_u^+$.

As far as the rotational energies are concerned, we make the further assumption that the molecule in the bound state can be treated as a rigid rotor also because the centrifugal stretching constant [38] of the bound state is not known. In this approximation, the rotational energy eigenvalues are written as

$$E_{J'} = B'_e J'(J'+1), \tag{4}$$

where $B'_e = \hbar^2 \big/ \left(2m_r R_{e'}^2\right)$ is the rotational constant. $m_r = 1.09 \times 10^{-25}$ kg is the average reduced mass of Xe in a sample of natural isotopic abundance. There is no need to calculate the rotational constant for different isotopes for several reasons. First of all, the contribution of rotations to the spectrum intensity is tiny. Moreover, the experimental signal is the convolution of the contributions due to all Xe isotopes in the sample. Finally, the resolution needed to discriminate the contributions of each isotope by far exceeds the available experimental resolution.

Finally, $|\epsilon'', J''\rangle$ represents a scattering state of kinetic energy ϵ'' and angular momentum J'' in the vibrational continuum of the dissociative potential.

The exponential prefactor in (1) accounts for the equilibrium thermal distribution of the rovibrational degrees of freedom. At room temperature, $\beta^{-1} \approx 208.5$ cm^{-1}.

The vibrational energy eigenvalues $E_{v'}$ and the vibrational eigenfunctions $|v', J'\rangle$ are found by numerically integrating the Schrödinger equation for the rotationless potential [38] using the Numerov–Cooley finite difference scheme [39] and replacing the centrifugal potential by the constant $B'_e J'(J'+1)$ for the reasons discussed above [36, 38].

The potential energy curve for the upper bound $(3)0_u^+$ state is reported in figure 2. The points are data taken from the literature [23]. For numerical purposes, the theoretical potential is accurately fitted to a Morse-type potential:

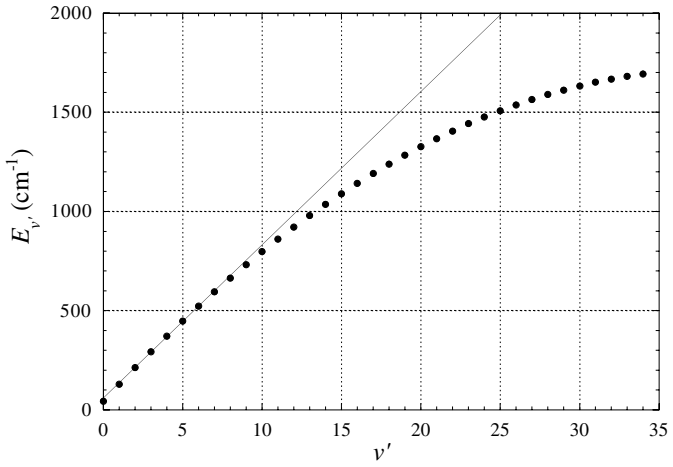

Figure 3. Energy eigenvalues of the bound potential V_b. The zero of energy is taken at the bottom of the potential well. The solid line represents the vibrational energy eigenvalues of a parabolic potential with the same curvature as that of the Morse potential at the equilibrium position.

$$V_b = T'_e + D'_e\{1 - \exp[-\beta_{e'}(R - R_{e'})]\}^2, \tag{5}$$

where D'_e is the well depth.

The values of the fitting parameters are $T'_e = 13\,860$ cm^{-1}, $D'_e = 1717$ cm^{-1}, $R_{e'} = 3.23$ Å and $\beta_{e'}R_{e'} = 6.734$. This fit is represented in figure 2 by the solid line. It describes quite well the position and strength of the minimum, the repulsive- and also the long-range behaviour of the potential. The largest deviation from the theoretical potential occurs between 4.5 and 5.5 Å. This is not very important for our purposes because, as we will see, only the lowest-lying vibrational states need to be considered.

This bound potential accommodates up to $v' \approx 34$ vibrational states though only the first ten significantly contribute to the spectrum owing to the Boltzmann factor. In figure 3 we report the energy eigenvalues $E_{v'}$ as a function of v', as measured from the bottom of the potential well. A solid line represents the vibrational energy eigenvalues for a purely parabolic potential with the same curvature, $2D'_e\beta^2_{e'}$, of the Morse potential at the equilibrium position. It can be easily concluded that a parabolic potential with the same position of the minimum and the same curvature of the actual Morse potential would give the same eigenvalues and eigenfunctions as the Morse potential itself for the first ten vibrational eigenstates. Thus, in our experimental conditions and for our purposes, the actual shape of the bound potential does not influence very much the Franck–Condon calculations provided that the values of the position of the minimum and the curvature at the minimum of the potential are the correct ones because only the first vibrational states are thermally excited.

The value of the rotational constant $B'_e \approx 2.47 \times 10^{-2}$ cm^{-1} corresponds to a rotational temperature $\Theta_r \approx 3.5 \times 10^{-2}$ K. Thus, for $T \approx 300$ K, states of quite high angular momentum J' are thermally excited. Their population is non-negligible for $J' \leqslant 250$ with average $\langle J' \rangle \approx 80$.

The scattering states $|\epsilon'', J''\rangle$ are found by numerically integrating the Schrödinger equation for the effective potential

$$V_{fJ}(R) = V_f(R) + \frac{\hbar^2}{2m_r R^2} J''(J'' + 1) \tag{6}$$

which includes the centrifugal contribution $\propto R^{-2}$.

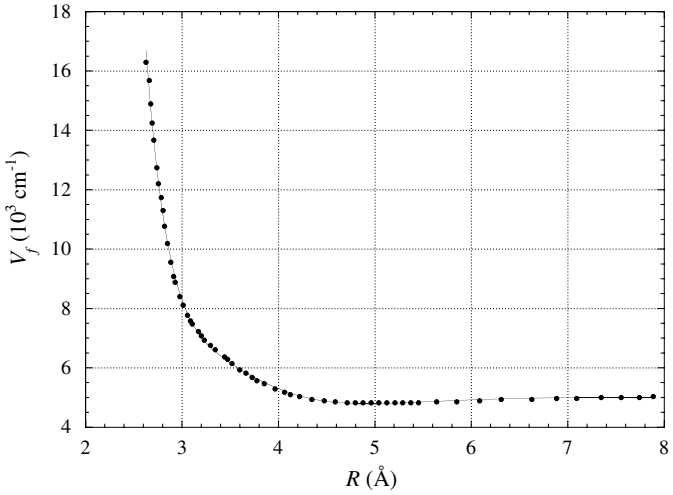

Figure 4. Potential energy curve for the (mainly) dissociative $(1)0_g^+$ state. Points: literature data [23]. Solid curve: HFD-B-type potential fit.

V_f is the potential of the (mainly) dissociative $(1)0_g^+$ state. It is characterized by a very shallow minimum of depth $D_e'' \approx 217.9$ cm^{-1} at the large distance $R_{e''} \approx 4.92$ Å and by $T_e'' \approx 4779.2$ cm^{-1}, measured from the same energy reference of the potential of the bound state [23]. In figure 4, the literature potential is represented by dots [23]. The theoretical potential is accurately fitted to the analytical form

$$V_f(R) = T_e'' + D_e'' f(x) \qquad (x = R/R_{e''}), \tag{7}$$

where $f(x)$ is a Hartree–Fock–dispersion (HFD) potential with its repulsive part described by an exponential term with adjustable slope (HFD-B-type potential) [40]

$$f(x) = f_1 + f_2 \mathrm{e}^{(-A_2x+A_3x^2)} - \mathrm{e}^{-(D/x-1)^2} \sum_{j=0}^{2} \frac{f_{2j+6}}{x^{2j+6}} \qquad \text{for} \quad x \leqslant 1.53. \tag{8}$$

The values of the fitting parameters are $f_1 = 0.756$, $f_2 = 2.552\,72 \times 10^4$, $A_2 = 3.352$, $A_3 = -15.497$, $D = 2.044$, $f_6 = -16.851$, $f_8 = 40.305$ and $f_{10} = -21.205$. For $x > 1.53$, i.e. for $R \geqslant 7.53$ Å, $f = 1$. The fitting function is plotted as a solid curve in figure 4.

The Schrödinger equation with this potential is integrated with a Runge–Kutta fourth-order scheme with adaptive stepsize control [41]. The scattering wavefunctions are normalized to unitary incoming flux [37]

$$\psi_{\epsilon''} = \langle R|\epsilon'', J''\rangle \xrightarrow{R\to\infty} \left(\frac{2m_r}{\pi\hbar^2 k}\right)^{1/2} \sin(kR + \eta), \tag{9}$$

where $\hbar^2k^2/2m_r = \epsilon''$ and η is the appropriate phase shift.

The overlap integrals occurring in (1) are evaluated by spline interpolation and quadrature [42]. The theoretical line shape is then convoluted with the instrumental function, which is a Gaussian of 16 cm^{-1} of full width at half maximum.

In figure 5, the simulated spectrum (dash-dotted line) is compared with the experimental one (thin solid line). The shape obtained using the literature potential for the $(1)0_g^+$ state only qualitatively agrees with the experiment. It is correctly stretched towards the blue side as a

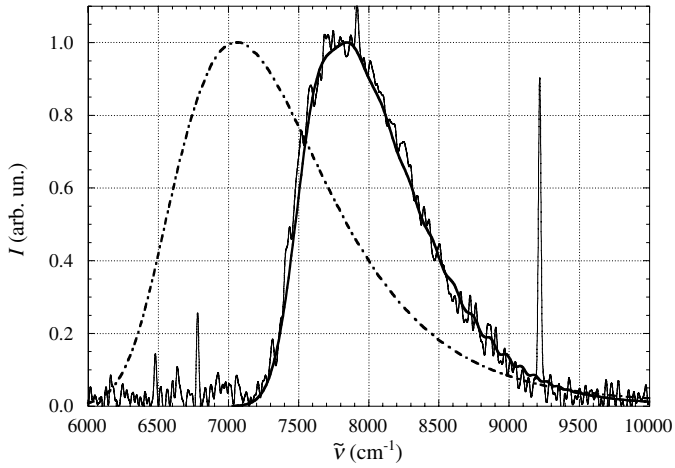

Figure 5. Experimental and simulated spectra. Thin solid line: experiment. Dash-dotted line: spectrum computed using the literature potential for the dissociative state [23]. Thick solid line: spectrum calculated using a R^{-12} repulsive potential with adjustable parameters.

consequence of the non-negligible contribution of vibrational states with $v' > 0$. However, its position is too strongly red shifted and its width is nearly twice as large as observed. We thus conclude that the potential energy curves of the bound and of the dissociative states are too close to each other and that the dissociative potential is too steep.

It is clear that either, or even both, theoretical potentials fail to reproduce the experimental result. One way to improve the situation could be to modify both potentials until the simulated spectrum reasonably agrees with the experiment. This possibility, however, opens up an infinite number of combinations and, thus, it does not make sense to pursue it any further.

On the other hand, owing to the fact that only the lowest vibrational levels of the upper bound potential are thermally excited, the actual shape of the bound potential does not influence very much the outcome of the calculations provided that the values of the position of the minimum and of the curvature at the minimum are correct. This consideration leads to the opportunity to modify only the potential of the lower state.

We thus safely assume that the upper bound state is correctly described by the literature potential [23]. The repulsive part of the lower potential can be determined by inverting the line shape [37]. To this goal, we assume that the lower state is described by the purely repulsive potential

$$V_{\mathrm{rep}} = A + \frac{V_0}{x^{12}} \qquad (x = R/R_{e'})\,. \tag{10}$$

Here, R is scaled by the equilibrium distance of the bound state just for numerical convenience.

A and V_0 are adjustable parameters to be determined by fitting the simulated spectrum to the observed one once the corresponding scattering wavefunctions are suitably computed. If the values $A = (5315 \pm 32)$ cm^{-1} and $V_0 = (760 \pm 16)$ cm^{-1} are used, the simulated spectrum (figure 5, thick solid line) perfectly agrees with the experiment. The uncertainties on A and V_0 reflect the uncertainty on the experimental determination of the position and width of the spectrum respectively.

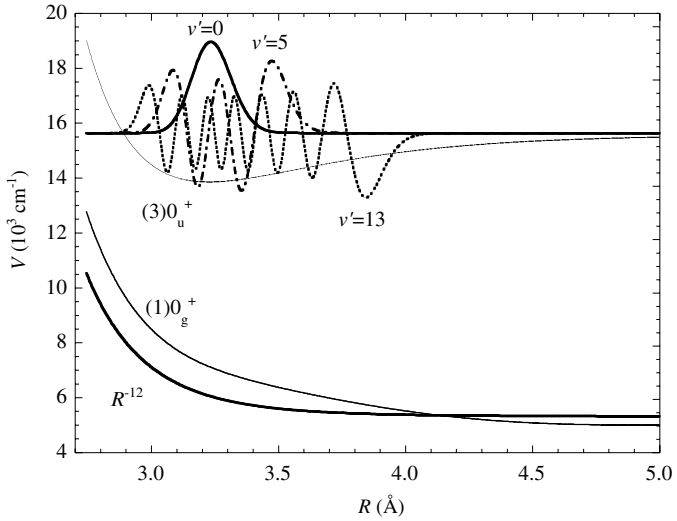

Figure 6. Potentials of the $(3)0_u^+$ and $(1)0_g^+$ states. Thin lines: literature potentials [23]. Thick line: best fit potential. The vibrational eigenfunctions for $v' = 0$, 5 and 13 are shown.

On the blue side, small wiggles in the simulated spectrum reflect the contributions of vibrational states with $v' \geqslant 10$. They are not observed because of an unfavourable signal-to-noise ratio and the Boltzmann factor.

In figure 6, we compare the literature potential of the lower state with the potential determined by the inversion procedure. The bound state is also shown with some vibrational eigenfunctions in order to visualize the coordinate range in which the Franck–Condon factors are non-negligible. The range, in which the comparison between the potentials describing the dissociative state is reasonable, is limited to $(2.7 \leqslant R \leqslant 4.5)$ Å because vibrational states with $v' \gg 10$ contribute little.

The difference between the best fit potential and the theoretical one for $R = R_{e'}$ is $\approx$880 cm^{-1}. No comparison can be made with the experimental determination of the dissociative potential of this state accomplished by REMPI techniques [26] because selective multiphoton excitation from the molecular ground-state samples the potential for much larger R than in the present case.

We believe that the energy difference determined in this way is large enough for theoreticians to improve the calculation of the potentials and of the transition moments. However, we must stress the fact that, in our analysis, we have chosen to consider exactly the theoretical potential of the bound state in order to modify the dissociative one.

Critical issues in our determination of the $(1)0_g^+$ state potential are the assumption of validity of the centroid approximation and the use of the literature potential for the $(3)0_u^+$ state. We can justify these assumptions only on the basis of Occam's razor [43], according to which entities should not be multiplied beyond necessity. However, the assumption that emission takes place from an excimer population in thermal equilibrium explains the observed blue asymmetry of the line shape and rules out the possibility that emission is produced by a transition from a vibrationally relaxed bound state because it would yield a line shape of opposity asymmetry than actually observed.

The present analysis could be confirmed by measuring the spectrum as a function of temperature in order to change the distribution of the rovibrational states. Moreover, this

experiment and its consequences open up the possibility of investigating higher lying excimer states in other rare gases that might also be of interest in astrophysics.

Acknowledgments

We acknowledge the invaluable support of D Iannuzzi, now at Vrije Universiteit, Amsterdam, The Netherlands.

References

[1] Rhodes C K (ed) 1979 *Excimer Lasers* (Berlin: Springer)
[2] Knoll G F 1989 *Radiation Detectors and Measurements* (New York: Wiley)
[3] Colli L 1954 *Phys. Rev.* **95** 892
[4] Brodmann R, Zimmerer G and Hahn U 1976 *Chem. Phys. Lett.* **41** 160
[5] Dutuit O, Gutcheck R A and Calvé J L 1978 *Chem. Phys. Lett.* **58** 66
[6] Gornik W, Matthias E and Schmidt D 1982 *J. Phys. B: At. Mol. Phys.* **15** 3413
[7] Dehmer P M, Pratt S T and Dehmer J L 1986 *J. Chem. Phys.* **85** 13
[8] Koehler H A, Federber L J, Redhead D L and Ebert P J 1974 *Phys. Rev.* A **9** 768
[9] Keto J W, Gleason R E and Walters G K 1979 *Phys. Rev. Lett.* **33** 1365
[10] Leichner P K, Palmer K F, Cook J D and Thieneman M 1976 *Phys. Rev.* A **13** 1787
[11] Wenck H D, Hasnain S S, Nikitin M M, Sommer K and Zimmerer G F K 1979 *Chem. Phys. Lett.* **66** 138
[12] Museur L, Kanaev A V, Zheng W Q and Castex M C 1994 *J. Chem. Phys.* **101** 10548
[13] Moutard P, Laporte P, Subtil J L, Damany N and Damany H 1988 *J. Chem. Phys.* **88** 7485
[14] Ledru G, Marchal F, Sewraj N, Salamero Y and Millet P 2006 *J. Phys. B: At. Mol. Opt. Phys.* **39** 2031
[15] Raymond T D, Bőwering N, Kuo C Y and Keto J W 1984 *Phys. Rev.* A **29** 721
[16] Millet P, Birot A, Brunet H, Galy J, Pons-Germain B and Teyssier J L 1978 *J. Chem. Phys.* **69** 92
[17] Brodmann R and Zimmerer G 1977 *J. Phys. B: At. Mol. Phys.* **10** 3395
[18] Bonifield T D, Rambow F H K, Walters G K, McCusker M V, Lorents D C and Gutcheck R A 1980 *J. Chem. Phys.* **72** 2914
[19] Salamero Y, Birot A, Brunet H, Galy J and Millet P 1984 *J. Chem. Phys.* **80** 4774
[20] Moutard P, Laporte P, Damany N, Subtil J L and Damany H 1986 *Chem. Phys. Lett.* **132** 521
[21] Alekseev V A and Setser D W 1999 *J. Phys. Chem.* A **103** 8396
[22] Ermler W C, Lee Y S, Pitzer K S and Winter N W 1978 *J. Chem. Phys.* **69** 976
[23] Jonin C and Spiegelmann F 2002 *J. Chem. Phys.* **117** 3059
[24] Mulliken R S 1970 *J. Chem. Phys.* **52** 5170
[25] Castex M C 1981 *J. Chem. Phys.* **74** 759
[26] Koeckhoven S M, Burma W J and de Lange C A 1995 *J. Chem. Phys.* **102** 4020
[27] Richmann M K, Nelson T O and Setser D W 1993 *Chem. Phys. Lett.* **210** 71
[28] Keto J W, Cai H, Kykta M, Lei C, Mőller T and Zimmerer G 1997 *J. Chem. Phys.* **107** 6080
[29] Belogurov S, Bressi G, Carugno G, Conti E, Iannuzzi D and Meneguzzo A T 2000 *Nucl. Instrum. Methods* A **452** 167
[30] Borghesani A F, Bressi G, Carugno G, Conti E and Iannuzzi D 2001 *J. Chem. Phys.* **115** 6042
[31] Palmer R A, Manning C J, Rzepiela J A, Widder J M and Chou J L 1989 *Appl. Spectrosc.* **43** 193
[32] Borghesani A F, Carugno G, Iannuzzi D and Mogentale I 2005 *Eur. Phys. J.* D **35** 299
[33] Jonin C, Laporte P and Saoudi R 1998 *J. Chem. Phys.* **108** 480
[34] Vallée O, Marié E, Minh N T and Vetter R 1981 *Phys. Rev.* A **24** 1391
[35] Bőwering N, Bruce M R and Keto J W 1986 *J. Chem. Phys.* **84** 709
[36] Herzberg G 1950 *Spectra of Diatomic Molecules* (Princeton, NJ: Van Nostrand-Reinhold)
[37] Tellinghuisen J 1985 *Photodissociation and Photoionization (Advances in Chemical Physics* vol LX*)* ed K P Lawley (New York: Wiley) pp 299–369
[38] Haken H and Wolf H C 2004 *Molecular Physics and Elements of Quantum Chemistry* (Berlin: Springer)
[39] Koonin S E and Meredith D C 1990 *Computational Physics* (Reading, MA: Addison-Wesley)
[40] Aziz R and Slaman M J 1986 *Mol. Phys.* **58** 679
[41] Press W H, Teukolsky S A, Vetterling W T and Flannery B P 1992 *Numerical Recipes in Fortran* (Cambridge: Cambridge University Press)
[42] Shampine L F and Allen R C 1973 *Numerical Computing: An Introduction* (Philadelphia, PA: Saunders)
[43] Priest G and Read S 1981 *Mind* **90** 274